MATERIALS SCIENCE

Erasable and recreatable two-dimensional electron gas at the heterointerface of $SrTiO_3$ and a water-dissolvable overlayer

Kun Han[1]*, Kaige Hu[2,3]*, Xiao Li[3,4], Ke Huang[1], Zhen Huang[5], Shengwei Zeng[5], Dongchen Qi[6,7], Chen Ye[1], Jian Yang[1], Huan Xu[8], Ariando Ariando[5], Jiabao Yi[9], Weiming Lü[10†], Shishen Yan[10], X. Renshaw Wang[1,8†]

Copyright © 2019 The Authors, some rights reserved; exclusive licensee American Association for the Advancement of Science. No claim to original U.S. Government Works. Distributed under a Creative Commons Attribution NonCommercial License 4.0 (CC BY-NC).

While benefiting greatly from electronics, our society also faces a major problem of electronic waste, which has already caused environmental pollution and adverse human health effects. Therefore, recyclability becomes a must-have feature in future electronics. Here, we demonstrate an erasable and recreatable two-dimensional electron gas (2DEG), which can be easily created and patterned by depositing a water-dissolvable overlayer of amorphous $Sr_3Al_2O_6$ (*a*-SAO) on $SrTiO_3$ (STO) at room temperature. The 2DEG can be repeatedly erased or recreated by depositing the *a*-SAO or dissolving in water, respectively. Photoluminescence results show that the 2DEG arises from the *a*-SAO–induced oxygen vacancy. Furthermore, by gradually depleting the 2DEG, a transition of nonlinear to linear Hall effect is observed, demonstrating an unexpected interfacial band structure. The convenience and repeatability in the creation of the water-dissolvable 2DEG with rich physics could potentially contribute to the exploration of next generation electronics, such as environment-friendly or water-soluble electronics.

INTRODUCTION

With the substantial and increasing demands of consumer electronics in today's society, electronic waste has become one of the fastest growing segments of environmental pollution (*1*–*3*). Therefore, the next generation of electronics with environment-friendly features, such as water dissolvability and recyclability, is in high demand. One of the possible approaches to realizing this prospect is the application of removable nontoxic materials in electronic devices, where functionalities can be created and removed by introducing and removing the material at will. However, thus far, a facile process of creation and removal of the material in electronics is still challenging to achieve.

$Sr_3Al_2O_6$ (SAO), which is easily dissolvable in water (*4*), allows a possibility to realize water-soluble or recyclable electronic devices. Recently, two-dimensional electron gases (2DEGs) have been facilely created and patterned at oxide heterointerfaces via room temperature deposition of various types of aluminum (Al)–based amorphous overlayers on $SrTiO_3$ (STO), such as $LaAlO_3$ (LAO), Al_2O_3, and $YAlO_3$ (*5*, *6*). The interfacial 2DEGs originate from the oxygen vacancies, which were created by the Al-induced redox reactions (*5*–*8*). However, in all these heterointerfaces, the defects, e.g., oxygen vacancies, are permanently constrained inside the heterostructures with fixed overlayers. This consequentially limits its application in recyclable electronics (*9*–*11*), despite the fact that the facile room temperature fabrication process of this 2DEG system is convenient and promising for future adoption of oxides in electronics and thermoelectrics (*5*). Fortunately, as Al is also a main element of the SAO, the SAO meets the criteria for the occurrence of the Al-induced redox reactions (*5*–*8*). Therefore, it is potentially feasible to easily create a tunable 2DEG by controlling the concentration and distribution of the oxygen vacancy using the SAO, while the inherent solubility of the SAO offers a possibility to explore future water-soluble or recyclable electronics (*12*–*15*).

In this work, we report an erasable and recreatable 2DEG at the heterointerface between a water-dissolvable amorphous $Sr_3Al_2O_6$ (*a*-SAO) overlayer and single-crystalline STO. In particular, the patterning, deposition, and dissolution of *a*-SAO thin film on STO substrate are all done at room temperature, leading to convenience and advantages in the fabrication and recycling processes. Furthermore, on the basis of photoluminescence (PL) measurement, we show that the 2DEG is induced by the oxygen vacancies at the interface, which could be conveniently removed by exposing the *a*-SAO overlayer in a humid environment, such as water or moisture. Last, during the *a*-SAO and oxygen vacancy removal process, a nonlinear-to-linear Hall resistance transition occurs and the 2DEG eventually completes a metal-to-insulator transition (MIT), which is well explained by a two-band model supported by the first-principles calculations.

RESULTS

Time-dependent electrical transport characterization

Various types of *a*-SAO/STO heterointerfaces were prepared at room temperature as described in Materials and Methods. The facile room temperature deposition is very beneficial to potential electronic applications. Additional amorphous LAO (*a*-LAO)/STO heterointerfaces

[1]School of Physical and Mathematical Sciences, Nanyang Technological University, 637371 Singapore, Singapore. [2]School of Physics and Optoelectronic Engineering, Guangdong University of Technology, Guangzhou 510006, China. [3]Department of Physics, University of Texas at Austin, Austin, TX 78712, USA. [4]Center for Quantum Transport and Thermal Energy Science, School of Physics and Technology, Nanjing Normal University, Nanjing 210023, China. [5]Department of Physics and NUSNNI-Nanocore, National University of Singapore, 117411 Singapore, Singapore. [6]ARC Centre of Excellence in Future Low-Energy Electronics Technologies, School of Chemistry, Physics, and Mechanical Engineering, Queensland University of Technology, Brisbane, Queensland 4001, Australia. [7]Department of Chemistry and Physics, La Trobe Institute for Molecular Science, La Trobe University, Melbourne, Victoria 3086, Australia. [8]School of Electrical and Electronic Engineering, Nanyang Technological University, 639798 Singapore, Singapore. [9]Global Innovative Centre for Advanced Nanomaterials, School of Engineering, The University of Newcastle, Callaghan New South Wales 2308 Australia. [10]Spintronics Institute, School of Physics and Technology, University of Jinan, Jinan 250022, China.
*These authors contributed equally to this work.
†Corresponding author. Email: sdy_lvwm@ujn.edu.cn (W.L.); renshaw@ntu.edu.sg (X.R.W.)

Downloaded from http://advances.sciencemag.org/ on August 29, 2019

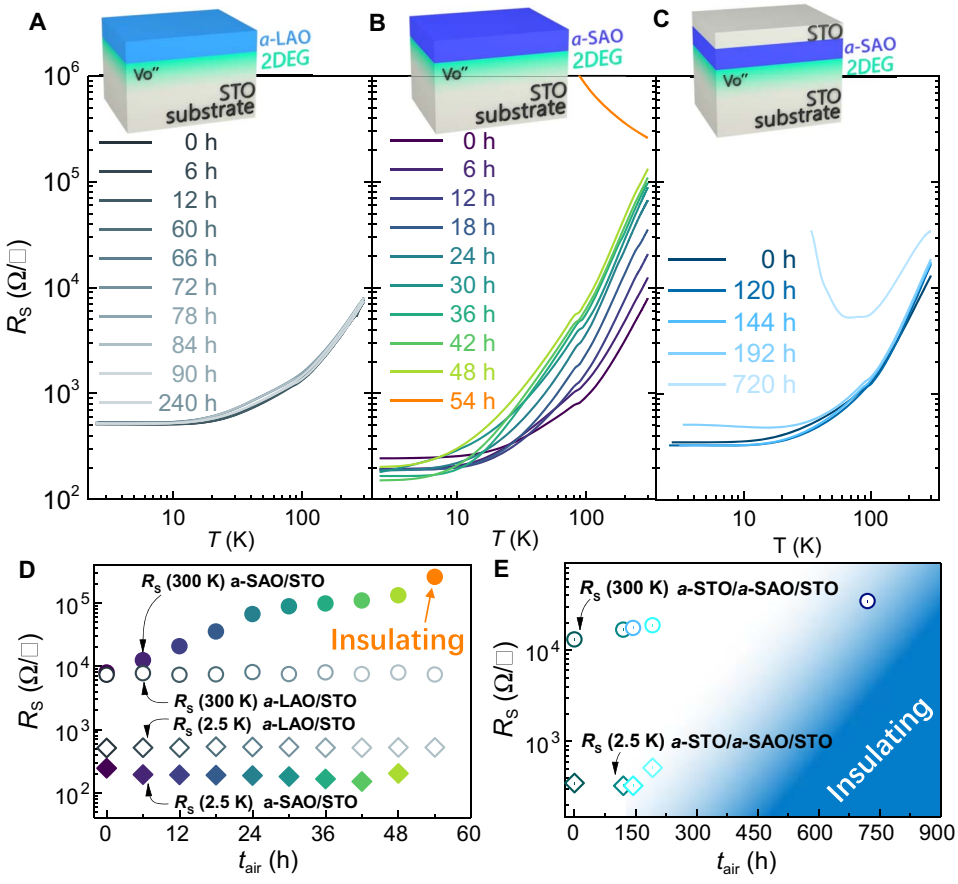

Fig. 1. Temperature-dependent transport property with different t_{air}. A 2DEG is formed at (**A**) the *a*-LAO/STO (001), (**B**) *a*-SAO/STO (001) interfaces, and (**C**) *a*-STO–capped *a*-SAO/STO (001). The 2DEG at the *a*-LAO/STO interface is much more stable than that at the *a*-SAO/STO interface under ambient conditions of room temperature and 70% of relative humidity. R_S as a function of t_{air} at 300 and 2.5 K for (**D**) 4-nm *a*-LAO/STO, 4-nm *a*-SAO/STO, and (**E**)10-nm *a*-STO–capped 4-nm *a*-SAO/STO, respectively. Inset: The schematic view of oxygen-vacancy–induced 2DEG exists at the (A) *a*-LAO/STO, (B) *a*-SAO/STO, and (C) *a*-STO–capped *a*-SAO/STO interfaces.

were also prepared as a control sample to study the transport behavior of the stable oxygen vacancy as a function of air exposure time (t_{air}). It has been reported that the epitaxial SAO single-crystal film is water soluble (*4*). Here, we found that the *a*-SAO thin film can also be easily dissolved in the deionized (DI) water. Figure 1 (A to C) shows the temperature-dependent sheet resistance, $R_S(T)$, of the 4-nm *a*-LAO/STO, 4-nm *a*-SAO/STO, and 10-nm amorphous STO (*a*-STO)–capped 4-nm *a*-SAO/STO interfaces in an ambient environment with a relative humidity of 70% and different t_{air}. Right after deposition, all interfaces exhibit a similar metallic behavior, including $R_S(T)$, carrier density (n_S), and carrier mobility (μ_H), in the entire temperature range of 2.5 to 300 K (see fig. S2). While the $R_S(T)$ of the metallic *a*-LAO/STO interface remains unchanged as t_{air} increases, the *a*-SAO/STO, however, is markedly affected by the exposure to ambient conditions, as illustrated in Fig. 1B. The metallic behavior ($dR_S/dT > 0$) of the 4-nm *a*-SAO/STO interface is preserved up to t_{air} = 48 hours, with marked changes in high-temperature R_S and negligible changes in low-temperature R_S. As t_{air} increases further (greater than 48 hours), the 4-nm *a*-SAO/STO interface exhibits an abrupt transition to a semiconducting behavior and eventually becomes insulating (see Fig. 1B). Therefore, we show that an MIT can be triggered by leaving the sample in air for a number of hours to absorb moisture from air. Furthermore, the MIT at the *a*-SAO/STO interface can be greatly slowed by capping a 10-nm *a*-STO thin film (Fig. 1C). Figure 1 (D and E) summarizes the t_{air} dependence of R_S(2.5 K) and R_S(300 K) of 4-nm *a*-LAO/STO, 4-nm *a*-SAO/STO, and 10-nm *a*-STO–capped 4-nm *a*-SAO/STO. A notable increase of R_S(300 K) by more than one order of magnitude can be seen in 4-nm *a*-SAO/STO by exposing under ambient conditions. In contrast, both R_S(2.5 K) of all heterointerfaces and the R_S(300 K) of both the 4-nm *a*-LAO/STO and 10-nm *a*-STO–capped 4-nm *a*-SAO/STO show almost t_{air}-independent behaviors ($t_{air} \leq 48$ hours), further confirming the correlation between the MIT and the removal of *a*-SAO.

Water-dissolvable and recyclable electronic devices

Because of the water solvability, recyclable electronic devices become possible with erasable and recreatable 2DEG enabled by adding or removing the *a*-SAO overlayer. A Hall bar device was built on the *a*-SAO/STO heterointerface using photolithography, and the *a*-SAO overlayer was then repeatedly removed and deposited. Figure 2B shows optical images of the Hall bar device with and without the *a*-SAO overlayer. The Hall bar device of the heterointerface experiences three states in each repetition, as schematically shown in Fig. 2C, namely, (i) just after growth (t = 0 min and 0 min < t < 30 min), (ii) one drop of DI water added onto the device to dissolve *a*-SAO (t = 30 min), and (iii) the *a*-SAO completely dissolved (30 min < t < 60 or 0 min). When the 20-nm *a*-SAO deposited on STO (t = 0 min), a 2DEG is created with a sheet conductance at 300 K, σ_S(300 K), of

Downloaded from http://advances.sciencemag.org/ on August 29, 2019

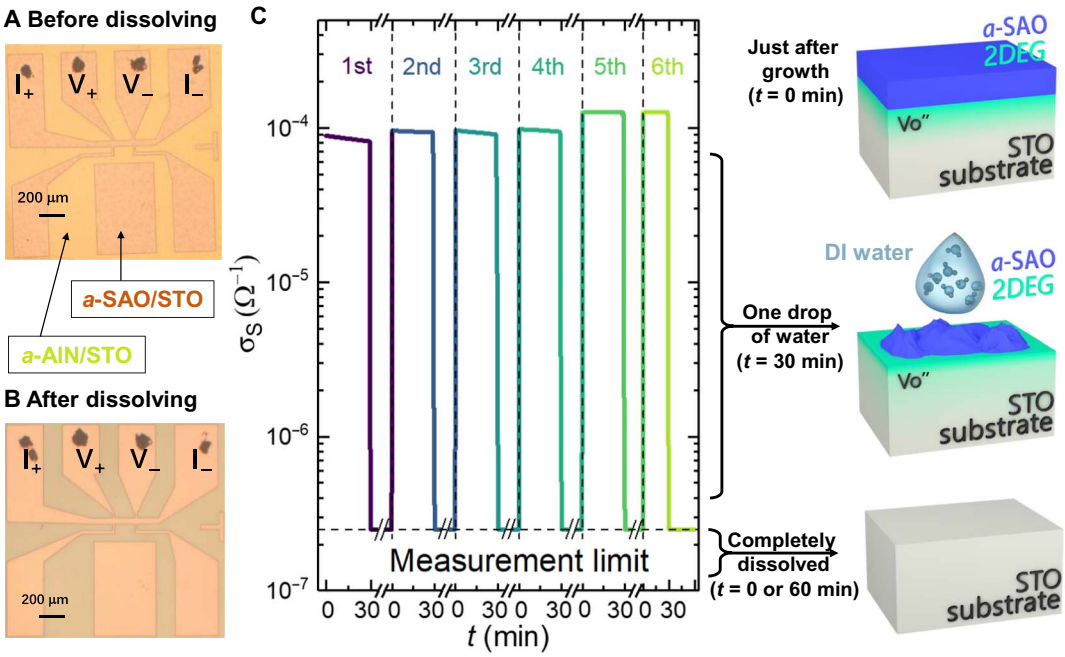

Fig. 2. Water-dissolvable and recyclable electronic devices. A 20-nm *a*-SAO/STO (001) heterointerface with a Hall bar pattern (**A**) before and (**B**) after the *a*-SAO overlayer dissolving into the DI water. The *a*-AlN in (A) denotes amorphous aluminium nitride. (**C**) Time dependence of sheet conductance, σ_S, at 300 K in ambient conditions for 20-nm *a*-SAO/STO (001). The vertical dash lines indicate that a drop of water was added on the Hall bar device, and the horizontal dash line indicates the measurement limit. The right panels schematically illustrated the three states of the electronic device: (top) metallic just after growth (at each $t = 0$ min), (middle) a fast MIT with one drop of DI water added on the device (at each $t = 30$ min), and (bottom) becoming insulating after the *a*-SAO fully dissolved into the DI water (at each 30 min < t < 60 or 0 min).

10^{-4} ohm^{-1}. At $t = 30$ min, a drop of DI water is added on the device. Note that the dissolution of SAO in water is a fast process. Therefore, a marked change of conductivity occurs almost instantaneously by adding one drop of DI water on top of the *a*-SAO/STO heterointerface, while the electrical transport varies gradually by exposing the *a*-SAO/STO heterointerface in the air (see Fig. 1D). This immediately removes the 2DEG with at least two orders of magnitude decrease in σ_S(300 K) down to the measurement limit. At 60 min (denoted as $t = 0$ min), the above process is repeated on the same device, and similar removal and recreation of 2DEG are demonstrated. Several repetitions of this process with a period of 1 hour are followed, which verifies the stability and repeatability of the electronic device (see Fig. 2C). In addition, during the practical implementation into a possible water-soluble electronic device, the key is to isolate the SAO and 2DEG from water or moisture. Fortunately, SAO is insoluble in organic solvent. Hence, the easiest method to the stability issues is to encapsulate the 2DEG with materials only soluble to a specific organic solvent. For example, polymethyl methacrylate is a versatile polymeric material and highly soluble in a solvent like acetone not water. Hence, with the help of one or several of these packaging materials, a water-soluble electronic device may be developed. Therefore, we demonstrate that the highly reproducible and reversible control of the 2DEG at the *a*-SAO/STO heterointerface by water dissolution provides a possibility to construct next generation electronic devices with environment-friendly features.

PL and the schematic mechanism of oxygen vacancies

Figure 3A shows the room temperature PL spectra of an as-received STO substrate, 4-nm *a*-LAO/STO, 4-nm *a*-SAO/STO, and 10-nm *a*-STO–capped *a*-SAO/STO under different treatments, including exposing to air and dissolving in water. In all the *a*-LAO/STO, *a*-SAO/STO, and *a*-STO–capped *a*-SAO/STO samples, a broad and intense PL emission centered at 430 nm (2.9 eV) was observed. This 2.9-eV PL peak corresponds to oxygen vacancies in STO (*8*, *16*). The *a*-SAO/STO, *a*-STO–capped *a*-SAO/STO, and *a*-LAO/STO all exhibit high PL intensity, indicating a high concentration of oxygen vacancies at the interfaces. Since all these samples show similar metallic behavior, we propose that the emergent conductivity in the *a*-SAO/STO interface right after the deposition also originates from oxygen vacancies at the surface of STO (see Fig. 3B). This is similar to that at the *a*-LAO/STO interface (*5*, *6*, *8*) and is further supported by the correlation between the interfacial conductivity and concentration of oxygen vacancy. The PL spectrum of the as-received insulating STO substrate was also measured as a baseline. We found that the baseline is a broad and weak PL peak at 415 nm (3.0 eV), due to the defects in the bulk of the as-received STO substrate created during the crystal growth (*8*, *16*). Because the defect density is very small, the as-received STO substrate is insulating. Therefore, using the PL spectrum of the as-received STO substrate as the baseline, any additional oxygen vacancies at the interface would produce a PL peak with a higher intensity than the baseline. As shown in Fig. 3A, after exposure to ambient conditions for 1 hour, the PL intensity of the *a*-SAO/STO interface notably decreases, demonstrating the effective removal of oxygen vacancies. This also eliminates the possibility of oxygen vacancies moving deeper into STO bulk in-gap state with lower energy (Fig. 3C) (*17*–*19*). This process at the *a*-SAO/STO interfaces can also be substantially accelerated by dissolving the *a*-SAO/STO sample in DI water (see fig. S3). Eventually, by dissolving in DI water, both *a*-SAO/STO and *a*-STO–capped *a*-SAO/STO heterointerfaces eventually become insulating with the final PL intensity the same as the PL baseline of

Downloaded from http://advances.sciencemag.org/ on August 29, 2019

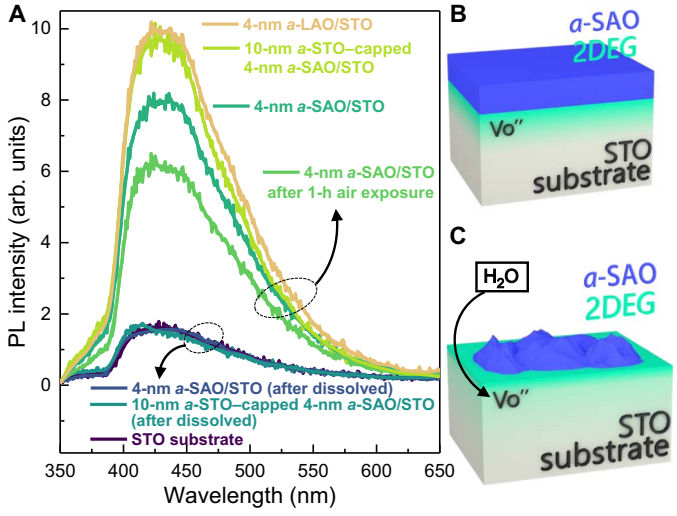

Fig. 3. Room temperature PL and the schematic mechanism of oxygen vacancies formed and filled near STO surface. (**A**) PL intensity of an as-received STO substrate, 4-nm *a*-LAO/STO, 4-nm *a*-SAO/STO, and 10-nm *a*-STO–capped 4-nm *a*-SAO/STO just after deposition, after 1 hour of air exposure and after dissolving in water. The illustration of the oxygen vacancies formed and filled near the surface of STO equilibrium: (**B**) between *a*-SAO film and its surface and (**C**) between the ambient conditions and its surface. The V_O″ represents oxygen vacancy occupying the in-gap state of STO, and the H_2O in the black squre box represents a water molecule under ambient conditions absorbed at the STO surface.

the as-received STO substrate. To summarize, as the *a*-SAO overlayer dissolves, the oxygen vacancy–related PL intensity is quenched, and the conductivity of the *a*-SAO/STO heterointerfaces vanishes. Therefore, we further conclude that the amount of oxygen vacancies at the *a*-SAO/STO heterointerface can be effectively controlled by removing the *a*-SAO overlayer and eventually determines the conductivity of the *a*-SAO/STO heterointerface.

There are three mechanisms that have been intensively discussed to explain the origin of 2DEG created at the heterointerface of amorphous/crystalline layer and STO, namely, (i) electronic reconstruction to resolve the polar catastrophe (*8*), (ii) thermal interdiffusion at the interface (*20*), and (iii) creation of oxygen vacancies in the STO substrate due to redox reaction (*5*, *6*, *8*). First, the macroscopic *a*-SAO grown on top of STO could be ordered on a local length scale (*21*). However, the *a*-SAO may not be a polar oxide because it does not have well-ordered crystalline $(LaO)^+$ or $(AlO_2)^-$ sublayers as the LAO. In addition, we performed an annealing experiment to exam the possibility of any polar catastrophe–related mechanism (*8*, *21*). We have prepared a crystalline SAO/STO (001) heterointerface at 760°C under oxygen partial pressure of 1×10^{-6} torr and then in situ annealed at 600°C for 1 hour in 1 bar of oxygen partial pressure to remove any oxygen vacancy. If the main origin is indeed the polar catastrophe, then the annealed crystalline SAO/STO heterointerface shall remain conducting (*8*). However, our annealed sample turns insulating. Therefore, the mechanism of polar catastrophe is experimentally ruled out. Second, an Al-doped STO ($SrTi_{1-x}Al_xO_{3-\delta}$) could be formed if the thermal interdiffusion of Ti and Al happens at the *a*-SAO/STO heterointerface. However, it is reported that $SrTi_{1-x}Al_xO_{3-\delta}$ has a bandgap of 3.5 eV, which is 0.3 eV larger than that of undoped STO (*22*). Hence, the second possible mechanism is also ruled out. Last, we propose that the most probable mechanism for the origin of 2DEG is the oxygen vacancies resulting from the Al-induced redox reactions (*5*, *6*, *8*). After adding the *a*-SAO layer, the interface becomes conducting because of the creation of oxygen vacancies. On the contrary, the interface becomes insulating because of the removal of oxygen vacancies by dissolving the *a*-SAO. This is consistent with the PL results in our study (see Fig. 3A).

Notably, this evolution of oxygen vacancy is in contrast to other previously reported STO-based amorphous 2DEG systems and our reference *a*-LAO/STO samples, where the $R_S(T)$ is stable (*5*). Normally, the oxygen vacancies are believed to remain in the STO after the removal of the *a*-SAO, because bulk oxygen vacancies are thermally stable at room temperature under ambient conditions. To be specific, oxygen atoms are expected to enter (or escape from) bulk STO only when both kinetic energy (typically >600°C) and oxidative (or reductive) conditions are simultaneously fulfilled (*5*, *23*, *24*). Hence, the results of t_{air}-dependent conductivity and PL demonstrate an unexpected feature of the oxygen vacancies at the surface of STO, namely, that the oxygen vacancies at the surface can be removed when exposed to the humid environment instead of being permanent, like the bulk defects.

The oxygen vacancies are removed by the oxygen atoms either from the DI water or ambient O_2. To identify the origin, we performed control experiments. First, we find that the R_S(300 K) of the 4-nm *a*-SAO/STO heterointerface is almost constant after a storage of 12 hours in both 1-atm pure O_2 and 1-atm pure N_2 at room temperature. Second, while the heterointerface is sealed in 1-atm N_2 environment, an abrupt MIT occurs only when a drop of DI water was added onto the surface. Hence, we can conclude that the oxygen atoms, which filling the oxygen vacancies, are from H_2O instead of the O_2 from air, as depicted in Fig. 3C. Previous studies have shown that the oxygen vacancies at the surface of many complex oxides, such as STO (*25*, *26*), TiO_2 (*27*, *28*), and $BaTiO_3$ (*25*, *29*), are immediately filled at room temperature when exposed to water. The presence of hydroxide ions on the oxide surfaces is revealed by both scanning tunneling microscopy (*27*) and x-ray photoelectron spectroscopy (*25*, *26*, *28*, *29*), which indicates that water dissociation at the oxygen vacancy into two hydroxide ions is an energetically favorable state (*27*, *29*). Hence, the most possible chemical reaction to fill the oxygen vacancy is $H_2O + V_O^{\bullet\bullet} + O_O^{\times} = 2(OH)_O^{\bullet}$. The equations are expressed in Kröger-Vink notation, where $V_O^{\bullet\bullet}$, $O_O^{\times}$, and $(OH)_O^{\bullet}$ denote oxygen vacancy, a lattice oxygen, and hydroxide ions occupying oxygen sites at the STO surface layer, respectively. In contrast, the conductance of both the reduced STO single-crystal substrate and oxygen-deficient thick STO film is stable, which is ascribed to the itinerant electrons buried deeply below the STO surface (*30*–*32*).

Two-band model

Unexpected complexity in the types, density, and mobility of the carriers can also be created at the *a*-SAO/STO heterointerface, depict of the mild room temperature deposition condition of *a*-SAO. Figure 4 shows the t_{air}-dependent Hall resistance data with extracted n_S and μ_S at T = 2.5 K. As the t_{air} increases, $R_{xy}(B)$ evolves from nonlinear (Fig. 4A) to almost linear behavior (Fig. 4B). In general, there are a number of possible origins of the nonlinear R_{xy}, including (i) anomalous Hall effect in ferromagnetic materials (*33*), (ii) magnetic-field–induced phase transition (*34*), (iii) spatially separated parallel conducting channels (*35*–*37*), and (iv) different orbital occupancies of multiple types of itinerant carriers (*14*, *38*, *39*). In our case, the first two mechanisms can be ruled out as the system showed neither signature of ferromagnetic order nor magnetic-field–induced phase transition. In the case of spatially separated parallel conducting channels, the different types of

Downloaded from http://advances.sciencemag.org/ on August 29, 2019

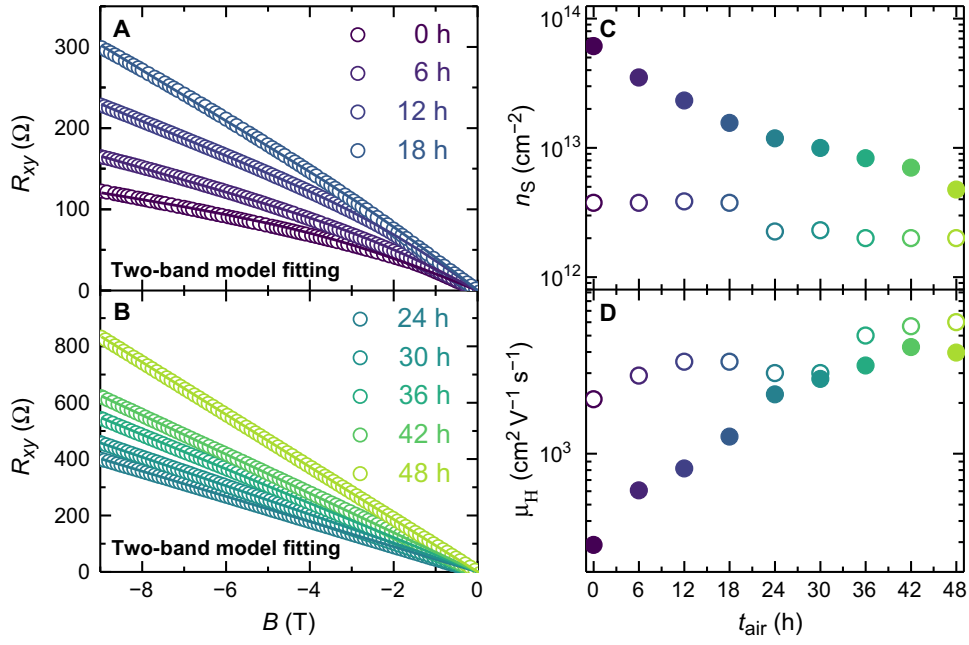

Fig. 4. Two-band model fitting of $R_{xy}(B)$ and t_{air}-dependent carrier density and mobility. Hall resistance of *a*-SAO/STO as a function of magnetic field at T = 2.5 K for various t_{air} (**A**) nonlinear and (**B**) almost linear Hall effect. The ring data points are the measured data, and the solid lines are fitted curves using the two-band model. The t_{air} dependence of carrier (**C**) densities and (**D**) mobilities at T = 2.5 K. Two types of electrons are denoted by n_1, n_2, μ_1, and μ_2.

charge carriers are generally spread in two different regions, i.e., the overlayer and the interface (*35*–*37*). However, in our *a*-SAO/STO samples, the only conducting region is the surface, and the multiple types of carriers are not expected to be spread widely. We, therefore, conclude that the different orbital occupancies of itinerant carriers are the only reasonable origin for the observed nonlinear Hall effect. This is also in good agreement with the previous studies on the (001)-oriented STO-based 2DEG systems, where the itinerant electrons occupy the states of Ti $3d_{xy}$ and $3d_{xz,yz}$ energy bands (*14*, *38*, *39*). The nonlinear Hall effect in both cases can be well fitted by a two-band model. In the two-band conduction model, there are two types of carriers coexisting at the interface, and thus, the R_{xy} and R_{xx} can be written as

$$R_{xy} = R_H B = \frac{(\mu_1^2 n_1 + \mu_2^2 n_2) + (\mu_1\mu_2 B)^2 (n_1 + n_2)}{e[(\mu_1 | n_1 | + \mu_2 | n_2 |)^2 + (\mu_1\mu_2 B)^2 (n_1 + n_2)^2]} B \quad (1)$$

and

$$R_{xx}(0) = \frac{1}{e(\mu_1 n_1 + \mu_2 n_2)} \quad (2)$$

where R_H is the Hall coefficient, and n_1, n_2 and μ_1, μ_2 are the densities and mobilities of the two types of carriers, respectively (*33*, *35*, *36*, *38*, *40*). As shown in Fig. 4A, the experimental data (hollow symbols) of the nonlinear R_{xy} can be fitted by Eq. 1 (solid lines) with two types of electrons. Figure 4 (C and D) summarizes the extracted two types of carrier density and carrier mobility as a function of t_{air} from 0 to 48 hours. We first focus our discussion on t_{air} from 0 to 18 hours. Figure 4 (C and D) shows that the minority electrons have a relatively constant density n_1 of 3.75×10^{12} cm^{-2} with mobility μ_1 slightly increasing from 2100 to 3500 cm^2 V^{-1} s^{-1}, whereas the majority of electrons have density n_2 decreasing from 6.12×10^{13} to 1.56×10^{13} cm^{-2} with mobility μ_2 notably increasing from 288 to 1261 cm^2 V^{-1} s^{-1}. In the process, as the *a*-SAO is gradually dissolved, the enhancement in the carrier mobility shall be attributed to the reduction of defect scattering (*13*) and electron-electron scattering (*41*, *42*). We note here the apparent appearance of a crossover point at t_{air} = 24 hours. For t_{air} longer than 24 hours, the electron mobility μ_1 and μ_2 becomes much closer. Providing $\mu_1 = \mu_2$, Eq. 1 can be simplified to $R_{xy} = \frac{1}{e(n_1+n_2)} B$, consistent with the almost linear B dependence of R_{xy} (Fig. 4B). Overall, n_1 changes slightly, while n_2 decreases more than one order of magnitude, accompanied by an increase in mobility for both carriers with μ_2 (2242 cm^2 V^{-1} s^{-1}) approaching μ_1 (3000 cm^2 V^{-1} s^{-1}) at the crossover point of t_{air} = 24 hours.

First-principles calculations

We propose that the evolution of multiple types of carriers is due to the change of the density of oxygen vacancies formed at the *a*-SAO/STO heterointerface. To clarify this, first-principles calculations on a $2 \times 2 \times 9$ supercell of cubic STO (space group $Pm\bar{3}m$, no. 221) with different number of oxygen vacancies were carried out to investigate the band structure. Figure 5 (A to D) shows the perfect supercell and that with one, two, and three oxygen vacancies, respectively, where, for clarity, only partial atoms of the supercell along the vertical direction are displayed. The corresponding band structures are plotted in Fig. 5 (E to H), along the high-symmetry point: M = (0.5, 0.5, 0), Γ = (0, 0, 0), and X = (0.5, 0, 0). It is apparent that, at the Γ point, there are two types of conduction bands near the Fermi energy with different symmetries are occupied. It turns out that the parabolic bands are of Ti $3d_{xy}$ character, and the asymmetry bands are of Ti $3d_{xz,yz}$ character. As we can see, the more oxygen vacancies at the heterointerface, the more Ti $3d_{xz,yz}$ orbitals are occupied. Moreover, the effective mass of electrons occupying the Ti $3d_{xy}$ orbital is lighter than that of electrons occupying the Ti $3d_{xz,yz}$ orbital, as the effective masses associated to different bands are proportional to the inverse of the second

Downloaded from http://advances.sciencemag.org/ on August 29, 2019

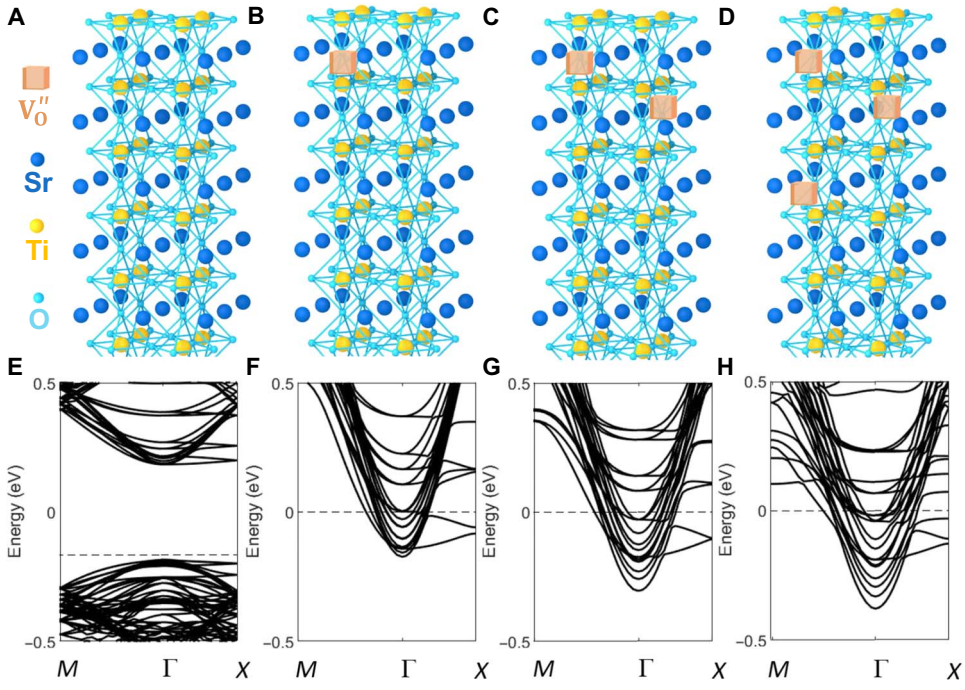

Fig. 5. First-principles calculations of electronic band structures of a 2 × 2 × 9 supercell of cubic STO with oxygen vacancies. Side view of the supercell structure with (**A**) zero, (**B**) one, (**C**) two, and (**D**) three vacancies, where, for clarity, only four layers along the vertical direction are shown. Corresponding band structures with (**E**) zero, (**F**) one, (**G**) two, and (**H**) three vacancies are also plotted, respectively.

derivative along Γ-*X* and Γ-*M* directions in the *k*-space (*43*, *44*). Therefore, on the basis of the orbital occupancies of the STO-based 2DEG systems (*14*, *37*, *38*, *45*–*49*), we conclude that the observed two types of electrons occupy different 3d orbitals: The first type of carriers with an almost constant carrier density (n_1) and higher mobility (μ_1) occupies the Ti $3d_{xy}$ subband, and the second type of carriers with a higher carrier density (n_2) and lower mobility (μ_2) occupies the Ti $3d_{xz,yz}$ subbands.

DISCUSSION

In summary, we present an erasable and recreatable 2DEG at the interface between water-dissolvable *a*-SAO and STO. This interfacial 2DEG is induced by oxygen vacancies at room temperature, which is verified by the PL measurement. Taking *a*-LAO/STO heterointerface with a stable 2DEG as a control sample, we speculate that the erasable 2DEG is due to the water solubility of *a*-SAO. During the dissolving process, the oxygen vacancies, which were created by *a*-SAO and are responsible for the occurrence of 2DEG, are refilled rapidly once exposed directly to the ambient conditions or water. Moreover, the removal rate of the oxygen vacancies is accompanied by the evolution of two types of carriers, demonstrating a tantalizing band structure in the easily created and patterned 2DEG. The facile process to erase and recreate 2DEG in this study is of possible help to the future novel electronics with environment-friendly features.

MATERIALS AND METHODS

Sample preparation

The *a*-LAO, *a*-SAO, and *a*-STO films were deposited under oxygen partial pressure of 1×10^{-6} torr by pulsed laser deposition using a KrF excimer laser (λ = 248 nm) with a repetition rate of 1 Hz and a laser fluence of 1.3 J/cm^2. For the STO substrates, a singly TiO_2 termination atomically flat surface was achieved by chemical etching and annealed at 950°C (*50*, *51*). Commercial LAO, STO single crystals, and sintered SAO ceramic were used as targets. Films deposited at room temperature showed an amorphous structure, which was confirmed by in situ reflection high-energy electron diffraction (RHEED). The growth rate was calibrated with the in situ RHEED oscillations obtained during the growth of single-crystalline SAO-STO samples (see fig. S1). All the amorphous films showed flat surfaces with a root mean square roughness less than 0.5 nm, as confirmed by atomic force microscopy (AFM).

Electronic transport and PL measurement

The sheet resistance and Hall effect were carried in a Quantum Design physical property measurement system with temperature range of 300 down to 2.5 K and magnetic fields up to 9 T. To determine the exact carrier density, a Hall bar pattern on STO substrate was prepared by a standard photolithography process. The PL spectra were carried at room temperature by a He-Cd laser with an excimer wavelength of 325 nm. A broad characteristic PL peak of oxygen vacancies centered at 430 nm (2.9 eV) was observed for different oxygen-deficient samples.

First-principles calculations

First-principles calculations were carried out using the Vienna Ab Initio Simulation Package (*52*) with the projector-augmented wave potentials (*53*). The kinetic energy cutoff is fixed to 520 eV, and the Monkhorst-Pack *k*-point mesh (*54*) is taken as 6 × 6 × 1. The coordinates and the cell shape were fully relaxed until the forces acting on the atoms are all smaller than 0.05 eV/Å.

Downloaded from http://advances.sciencemag.org/ on August 29, 2019

SUPPLEMENTARY MATERIALS

Supplementary material for this article is available at http://advances.sciencemag.org/cgi/content/full/5/8/eaaw7286/DC1

Section S1. RHEED oscillations of 4 unit cells (uc) of SAO/STO (001)
Section S2. Electrical transport properties of 4-nm *a*-SAO/STO and 4-nm *a*-LAO/STO
Section S3. Microscopy images of 20-nm *a*-SAO/STO (001) before and after dissolving into the DI water
Section S4. Microscopy images of 20-nm *a*-SAO/STO sample with different t_{air}
Section S5. Electrical transport properties of 4-nm *a*-SAO/STO with different t_{air}
Section S6. t_{air} dependence of R_S for 50-nm *a*-SAO/STO (001) and 10-nm *a*-STO–capped 4-nm *a*-SAO/STO
Section S7. Nonlinear to linear Hall effect of 4-nm *a*-SAO/STO heterointerface with different t_{air}
Section S8. Magnetoresistance of 4-nm *a*-SAO/STO with different t_{air}
Section S9. Growth oxygen partial pressure dependence of R_S
Section S10. AFM images of reusable STO surface topography
Section S11. Discussion of the possible chemical reactions to dissolve *a*-SAO and remove oxygen vacancies at STO surface by water
Fig. S1. RHEED oscillations of 4 uc of single-crystalline SAO grown on STO (001).
Fig. S2. Electrical transport properties of 4-nm *a*-SAO/STO and 4-nm *a*-LAO/STO.
Fig. S3. Microscopy images of 20-nm *a*-SAO/STO (001) with Hall bar pattern.
Fig. S4. Microscopy images of the surface of 20-nm *a*-SAO/STO sample with different t_{air}.
Fig. S5. Electrical transport properties of 4-nm *a*-SAO/STO with different t_{air}.
Fig. S6. t_{air} dependence of R_S.
Fig. S7. Nonlinear to linear Hall effect of 4-nm *a*-SAO/STO heterointerface.
Fig. S8. Magnetoresistance of 4-nm *a*-SAO/STO at 2.5 K with different t_{air}.
Fig. S9. Growth oxygen partial pressure dependence of R_S at 300 K.
Fig. S10. AFM images of reusable STO surface topography.

REFERENCES AND NOTES

1. B. H. Robinson, E-waste: An assessment of global production and environmental impacts. *Sci. Total Environ.* **408**, 183–191 (2009).
2. K. Zhang, J. L. Schnoor, E. Y. Zeng, E-waste recycling: Where does it go from here? *Environ. Sci. Technol.* **46**, 10861–10867 (2012).
3. Z. Wang, B. Zhang, D. Guan, Take responsibility for electronic-waste disposal. *Nature* **536**, 23–25 (2016).
4. D. Lu, D. J. Baek, S. S. Hong, L. F. Kourkoutis, Y. Hikita, H. Y. Hwang, Synthesis of freestanding single-crystal perovskite films and heterostructures by etching of sacrificial water-soluble layers. *Nat. Mater.* **15**, 1255–1260 (2016).
5. Y. Chen, N. Pryds, J. E. Kleibeuker, G. Koster, J. Sun, E. Stamate, B. Shen, G. Rijnders, S. Linderoth, Metallic and insulating interfaces of amorphous $SrTiO_3$-based oxide heterostructures. *Nano Lett.* **11**, 3774–3778 (2011).
6. S. W. Lee, Y. Liu, J. Heo, R. G. Gordon, Creation and control of two-dimensional electron gas using Al-based amorphous Oxides/SrTiO3Heterostructures grown by atomic layer deposition. *Nano Lett.* **12**, 4775–4783 (2012).
7. Q. Fu, T. Wagner, Interaction of nanostructured metal overlayers with oxide surfaces. *Surf. Sci. Rep.* **62**, 431–498 (2007).
8. Z. Q. Liu, C. J. Li, W. M. Lü, X. H. Huang, Z. Huang, S. W. Zeng, X. P. Qiu, L. S. Huang, A. Annadi, J. S. Chen, J. M. D. Coey, T. Venkatesan, Ariando, Origin of the two-dimensional electron gas at $LaAlO_3/SrTiO_3$ interfaces: The role of oxygen vacancies and electronic reconstruction. *Phys. Rev. X.* **3**, 021010 (2013).
9. C. Lin, A. A. Demkov, Electron correlation in oxygen vacancy in $SrTiO_3$. *Phys. Rev. Lett.* **111**, 217601 (2013).
10. C. Lin, C. Mitra, A. A. Demkov, Orbital ordering under reduced symmetry in transition metal perovskites: Oxygen vacancy in $SrTiO_3$. *Phys. Rev. B.* **86**, 161102 (2012).
11. M. Gu, J. Wang, X. S. Wu, G. P. Zhang, Stabilities of the intrinsic defects on $SrTiO_3$ surface and $SrTiO_3/LaAlO_3$ interface. *J. Phys. Chem. C* **116**, 24993–24998 (2012).
12. K. Eom, E. Choi, M. Choi, S. Han, H. Zhou, J. Lee, Oxygen vacancy linear clustering in a perovskite oxide. *J. Phys. Chem. Lett.* **8**, 3500–3505 (2017).
13. M. Huijben, G. Koster, M. K. Kruize, S. Wenderich, J. Verbeeck, S. Bals, E. Slooten, B. Shi, H. J. A. Molegraaf, J. E. Kleibeuker, S. van Aert, J. B. Goedkoop, A. Brinkman, D. H. A. Blank, M. S. Golden, G. van Tendeloo, H. Hilgenkamp, G. Rijnders, Defect engineering in oxide heterostructures by enhanced oxygen surface exchange. *Adv. Funct. Mater.* **23**, 5240–5248 (2013).
14. W. Niu, Y. Zhang, Y. Gan, D. V. Christensen, M. V. Soosten, E. J. Garcia-Suarez, A. Riisager, X. Wang, Y. Xu, R. Zhang, N. Pryds, Y. Chen, Giant tunability of the two-dimensional electron gas at the interface of γ-$Al_2O_3/SrTiO_3$. *Nano Lett.* **17**, 6878–6885 (2017).
15. B. W. Veal, S. K. Kim, P. Zapol, H. Iddir, P. M. Baldo, J. A. Eastman, Interfacial control of oxygen vacancy doping and electrical conduction in thin film oxide heterostructures. *Nat. Commun.* **7**, 11892 (2016).
16. D. Kan, T. Terashima, R. Kanda, A. Masuno, K. Tanaka, S. Chu, H. Kan, A. Ishizumi, Y. Kanemitsu, Y. Shimakawa, M. Takano, Blue-light emission at room temperature from Ar^+-irradiated $SrTiO_3$. *Nat. Mater.* **4**, 816–819 (2005).
17. A. Ohtomo, H. Y. Hwang, Surface depletion in doped $SrTiO_3$ thin films. *Appl. Phys. Lett.* **84**, 1716–1718 (2004).
18. B. Bryant, C. Renner, Y. Tokunaga, Y. Tokura, G. Aeppli, Imaging oxygen defects and their motion at a manganite surface. *Nat. Commun.* **2**, 212–216 (2011).
19. N. Poccia, M. Fratini, A. Ricci, G. Campi, L. Barba, A. Vittorini-Orgeas, G. Bianconi, G. Aeppli, A. Bianconi, Evolution and control of oxygen order in a cuprate superconductor. *Nat. Mater.* **10**, 733–736 (2011).
20. P. R. Willmott, S. A. Pauli, R. Herger, C. M. Schlepütz, D. Martoccia, B. D. Patterson, B. Delley, R. Clarke, D. Kumah, C. Cionca, Y. Yacoby, Structural basis for the conducting interface between $LaAlO_3$ and $SrTiO_3$. *Phys. Rev. Lett.* **99**, 155502 (2007).
21. Y. Z. Chen, F. Trier, T. Wijnands, R. J. Green, N. Gauquelin, R. Egoavil, D. V. Christensen, G. Koster, M. Huijben, N. Bovet, S. Macke, F. He, R. Sutarto, N. H. Andersen, J. A. Sulpizio, M. Honig, G. E. D. K. Prawiroatmodjo, T. S. Jespersen, S. Linderoth, S. Ilani, J. Verbeeck, G. van Tendeloo, G. Rijnders, G. A. Sawatzky, N. Pryds, Extreme mobility enhancement of two-dimensional electron gases at oxide interfaces by charge-transfer-induced modulation doping. *Nat. Mater.* **14**, 801–806 (2015).
22. A. B. Posadas, C. Lin, A. A. Demkov, S. Zollner, Bandgap engineering in perovskite oxides: Al-doped $SrTiO_3$. *Appl. Phys. Lett.* **103**, 142906 (2013).
23. D. V. Christensen, M. von Soosten, F. Trier, T. S. Jespersen, A. Smith, Y. Chen, N. Pryds, Controlling the carrier density of $SrTiO_3$-based heterostructures with annealing. *Adv. Electron. Mater.* **3**, 1700026 (2017).
24. A. Kalabukhov, R. Gunnarsson, J. Börjesson, E. Olsson, T. Claeson, D. Winkler, Effect of oxygen vacancies in the $SrTiO_3$ substrate on the electrical properties of the $LaAlO_3/SrTiO_3$ interface. *Phys. Rev. B.* **75**, 121404 (2007).
25. N. Domingo, E. Pach, K. Cordero-Edwards, V. Pérez-Dieste, C. Escudero, A. Verdaguer, Water adsorption, dissociation and oxidation on $SrTiO_3$ and ferroelectric surfaces revealed by ambient pressure X-ray photoelectron spectroscopy. *Phys. Chem. Chem. Phys.* **21**, 4920–4930 (2019).
26. W. Li, S. Liu, S. Wang, Q. Guo, J. Guo, The roles of reduced Ti cations and oxygen vacancies in water adsorption and dissociation on $SrTiO_3$(110). *J. Phys. Chem. C* **118**, 2469–2474 (2014).
27. R. Schaub, P. Thostrup, N. Lopez, E. Lægsgaard, I. Stensgaard, J. K. Nørskov, F. Besenbacher, Oxygen vacancies as active sites for water dissociation on rutile TiO_2(110). *Phys. Rev. Lett.* **87**, 266104 (2001).
28. G. Ketteler, S. Yamamoto, H. Bluhm, K. Andersson, D. E. Starr, D. F. Ogletree, H. Ogasawara, A. Nilsson, M. Salmeron, The nature of water nucleation sites on TiO_2(110) surfaces revealed by ambient pressure X-ray photoelectron spectroscopy. *J. Phys. Chem. C* **111**, 8278–8282 (2007).
29. J. L. Wang, F. Gaillard, A. Pancotti, B. Gautier, G. Niu, B. Vilquin, V. Pillard, G. L. M. P. Rodrigues, N. Barrett, Chemistry and atomic distortion at the surface of an epitaxial $BaTiO_3$ thin film after dissociative adsorption of water. *J. Phys. Chem. C* **116**, 21802–21809 (2012).
30. J. F. Schooley, W. R. Hosler, M. L. Cohen, Superconductivity in semiconducting $SrTiO_3$. *Phys. Rev. Lett.* **12**, 474–475 (1964).
31. O. N. Tufte, P. W. Chapman, Electron mobility in semiconducting strontium titanate. *Phys. Rev.* **155**, 796–802 (1967).
32. Z. Q. Liu, D. P. Leusink, X. Wang, W. M. Lü, K. Gopinadhan, A. Annadi, Y. L. Zhao, X. H. Huang, S. W. Zeng, Z. Huang, A. Srivastava, S. Dhar, T. Venkatesan, Ariando, Metal-insulator transition in $SrTiO_{3-x}$ thin films induced by frozen-out carriers. *Phys. Rev. Lett.* **107**, 146802 (2011).
33. A. Joshua, S. Pecker, J. Ruhman, E. Altman, S. Ilani, A universal critical density underlying the physics of electrons at the $LaAlO_3/SrTiO_3$ interface. *Nat. Commun.* **3**, 1129 (2012).
34. J. Biscaras, N. Bergeal, S. Hurand, C. Grossetête, A. Rastogi, R. C. Budhani, D. LeBoeuf, C. Proust, J. Lesueur, Two-dimensional superconducting phase in $LaTiO_3/SrTiO_3$ heterostructures induced by high-mobility carrier doping. *Phys. Rev. Lett.* **108**, 247004 (2012).
35. S.-Y. Hsu, J. M. Valles Jr., Observation of a well defined transition from weak to strong localization in two dimensions. *Phys. Rev. Lett.* **74**, 2331–2334 (1995).
36. T. F. Rosenbaum, S. B. Field, D. A. Nelson, P. B. Littlewood, Magnetic-field-induced localization transition in HgCdTe. *Phys. Rev. Lett.* **54**, 241–244 (1985).
37. J. S. Kim, S. S. A. Seo, M. F. Chisholm, R. K. Kremer, H.-U. Habermeier, B. Keimer, H. N. Lee, Nonlinear Hall effect and multichannel conduction in $LaTiO_3/SrTiO_3$ superlattices. *Phys. Rev. B.* **82**, 201407 (2010).
38. X. Renshaw Wang, L. Sun, Z. Huang, W. M. Lü, M. Motapothula, A. Annadi, Z. Q. Liu, S. W. Zeng, T. Venkatesan, Ariando, Parallel charge sheets of electron liquid and gas in $La_{0.5}Sr_{0.5}TiO_3/SrTiO_3$ heterostructures. *Sci. Rep.* **5**, 18282 (2015).
39. C. M. Hurd, *The Hall Effect in Metals and Alloys* (Plenum Press New York, 1972).
40. K. Han, Z. Huang, S. W. Zeng, M. Yang, C. J. Li, W. X. Zhou, X. Renshaw Wang, T. Venkatesan, J. M. D. Coey, M. Goiran, W. Escoffier, Ariando, Electrical properties and

Downloaded from http://advances.sciencemag.org/ on August 29, 2019

subband occupancy at the (La,Sr) (Al,Ta) $O_3/SrTiO_3$ interface. *Phys. Rev. Mater.* **1**, 011601 (2017).
41. G. Cheng, M. Tomczyk, A. B. Tacla, H. Lee, S. Lu, J. P. Veazey, M. Huang, P. Irvin, S. Ryu, C.-B. Eom, A. Daley, D. Pekker, J. Levy, Tunable electron-electron interactions in $LaAlO_3/SrTiO_3$ nanostructures. *Phys. Rev. X.* **6**, 041042 (2016).
42. X. Lin, B. Fauqué, K. Behnia, Scalable T^2 resistivity in a small single-component Fermi surface. *Science* **349**, 945–948 (2015).
43. A. Janotti, D. Steiauf, C. G. Van de Walle, Strain effects on the electronic structure of $SrTiO_3$: Toward high electron mobilities. *Phys. Rev. B.* **84**, 201304 (2011).
44. Z. Zhong, P. Wissgott, K. Held, G. Sangiovanni, Microscopic understanding of the orbital splitting and its tuning at oxide interfaces. *Europhys. Lett.* **99**, 37011 (2012).
45. M. Salluzzo, J. C. Cezar, N. B. Brookes, V. Bisogni, G. M. De Luca, C. Richter, S. Thiel, J. Mannhart, M. Huijben, A. Brinkman, G. Rijnders, G. Ghiringhelli, Orbital reconstruction and the two-dimensional electron gas at the $LaAlO_3/SrTiO_3$ interface. *Phys. Rev. Lett.* **102**, 166804 (2009).
46. G. Herranz, G. Singh, N. Bergeal, A. Jouan, J. Lesueur, J. Gázquez, M. Varela, M. Scigaj, N. Dix, F. Sánchez, J. Fontcuberta, Engineering two-dimensional superconductivity and Rashba spin-orbit coupling in $LaAlO_3/SrTiO_3$ quantum wells by selective orbital occupancy. *Nat. Commun.* **6**, 6028 (2015).
47. Y. Cao, X. Liu, P. Shafer, S. Middey, D. Meyers, M. Kareev, Z. Zhong, J.-W. Kim, P. J. Ryan, E. Arenholz, J. Chakhalian, Anomalous orbital structure in a spinel-perovskite interface. *npj Quantum Mater.* **1**, 16009 (2016).
48. X. Chi, Z. Huang, T. C. Asmara, K. Han, X. Yin, X. Yu, C. Diao, M. Yang, D. Schmidt, P. Yang, P. E. Trevisanutto, T. J. Whitcher, T. Venkatesan, M. B. H. Breese, Ariando, A. Rusydi, Large enhancement of 2D electron gases mobility induced by interfacial localized electron screening effect. *Adv. Mater.* **30**, 1707428 (2018).
49. J. Park, B.-G. Cho, K. D. Kim, J. Koo, H. Jang, K.-T. Ko, J.-H. Park, K.-B. Lee, J.-Y. Kim, D. R. Lee, C. A. Burns, S. S. A. Seo, H. N. Lee, Oxygen-vacancy-induced orbital reconstruction of Ti ions at the interface of $LaAlO_3/SrTiO_3$ heterostructures: A resonant soft-X-ray scattering study. *Phys. Rev. Lett.* **110**, 017401 (2013).
50. G. Koster, B. L. Kropman, G. J. H. M. Rijnders, D. H. A. Blank, H. Rogalla, Quasi-ideal strontium titanate crystal surfaces through formation of strontium hydroxide. *Appl. Phys. Lett.* **73**, 2920–2922 (1998).
51. M. Kawasaki, K. Takahashi, T. Maeda, R. Tsuchiya, M. Shinohara, O. Ishiyama, T. Yonezawa, M. Yoshimoto, H. Koinuma, Atomic control of the $SrTiO_3$ crystal surface. *Science* **266**, 1540–1542 (1994).
52. G. Kresse, J. Furthmüller, Efficient iterative schemes for ab initio total-energy calculations using a plane-wave basis set. *Phys. Rev. B.* **54**, 11169–11186 (1996).
53. G. Kresse, D. Joubert, From ultrasoft pseudopotentials to the projector augmented-wave method. *Phys. Rev. B.* **59**, 1758–1775 (1999).
54. H. J. Monkhorst, J. D. Pack, Special points for Brillouin-zone integrations. *Phys. Rev. B.* **13**, 5188–5192 (1976).

Acknowledgments: We thank C. Mun Yin and K. Onggadinata for their fruitful discussion. **Funding:** X.R.W. acknowledges supports from the Nanyang Assistant Professorship grant from Nanyang Technological University and Academic Research Fund Tier 1 (RG108/17 and RG177/18) and Tier 3 (MOE2018-T3-1-002) from Singapore Ministry of Education. K. Hu acknowledges financial support from National Natural Science Foundation of China (grant no. 11647108) and the China Scholarship Council (grant no. 201808440038). Z.H., S.Z., and A.A. acknowledge the support from the NUS Academic Research Fund (AcRF Tier 1 grant nos. R-144-000-391-114 and R-144-000-364-112) and the Singapore National Research Foundation (NRF) under the Competitive Research Programs (CRP grant no. NRF-CRP15-2015-01). D.Q. and J.Y. acknowledge the support of the Australian Research Council (grant no. FT160100207 and FT160100205, respectively). **Author contributions:** X.R.W., W.L., and K.Ha. conceived and designed the experiments. K.Ha., Z.H., and S.Z. prepared the samples and performed the electrical transport property measurements. K.Hua., C.Y., and J.Ya. performed the room temperature PL measurement. K. Hu and X.L. carried out the first-principles calculations. All authors contributed to the discussion and interpretation of the results. K.Ha., W.L., and X.R.W. wrote the manuscript with help from all other authors. **Competing interests:** The authors declare that they have no competing interests. **Data and materials availability:** All data needed to evaluate the conclusions in the paper are present in the paper and/or the Supplementary Materials. Additional data related to this paper may be requested from the authors.

Submitted 19 January 2019
Accepted 11 July 2019
Published 16 August 2019
10.1126/sciadv.aaw7286

Citation: K. Han, K. Hu, X. Li, K. Huang, Z. Huang, S. Zeng, D. Qi, C. Ye, J. Yang, H. Xu, A. Ariando, J. Yi, W. Lü, S. Yan, X. R. Wang, Erasable and recreatable two-dimensional electron gas at the heterointerface of $SrTiO_3$ and a water-dissolvable overlayer. *Sci. Adv.* **5**, eaaw7286 (2019).

Downloaded from http://advances.sciencemag.org/ on August 29, 2019

ScienceAdvances

Erasable and recreatable two-dimensional electron gas at the heterointerface of $SrTiO_3$ and a water-dissolvable overlayer

Kun Han, Kaige Hu, Xiao Li, Ke Huang, Zhen Huang, Shengwei Zeng, Dongchen Qi, Chen Ye, Jian Yang, Huan Xu, Ariando Ariando, Jiabao Yi, Weiming Lü, Shishen Yan and X. Renshaw Wang

Sci Adv **5** (8), eaaw7286.
DOI: 10.1126/sciadv.aaw7286

ARTICLE TOOLS http://advances.sciencemag.org/content/5/8/eaaw7286

SUPPLEMENTARY MATERIALS http://advances.sciencemag.org/content/suppl/2019/08/12/5.8.eaaw7286.DC1

REFERENCES This article cites 53 articles, 2 of which you can access for free
http://advances.sciencemag.org/content/5/8/eaaw7286#BIBL

PERMISSIONS http://www.sciencemag.org/help/reprints-and-permissions

Use of this article is subject to the Terms of Service

Science Advances (ISSN 2375-2548) is published by the American Association for the Advancement of Science, 1200 New York Avenue NW, Washington, DC 20005. 2017 © The Authors, some rights reserved; exclusive licensee American Association for the Advancement of Science. No claim to original U.S. Government Works. The title *Science Advances* is a registered trademark of AAAS.

Downloaded from http://advances.sciencemag.org/ on August 29, 2019